The effects of dynamic optical properties during interstitial laser photocoagulation

Megumi N Iizuka†, I Alex Vitkin†, Michael C Kolios‡ and Michael D Sherar†

† The Ontario Cancer Institute and Department of Medical Biophysics, University of Toronto, 610 University Avenue, Toronto, Ontario M5G-2M9, Canada
‡ Department of Mathematics, Physics and Computer Science, Ryerson Polytechnic University, Toronto, Ontario M5B 2K3, Canada

Abstract. A nonlinear mathematical model was developed and experimentally validated to investigate the effects of changes in optical properties during interstitial laser photocoagulation (ILP). The effects of dynamic optical properties were calculated using the Arrhenius damage model, resulting in a nonlinear optothermal response. This response was experimentally validated by measuring the temperature rise in albumen and polyacrylamide phantoms. A theoretical study of ILP in liver was conducted constraining the peak temperatures below the vaporization threshold. The temperature predictions varied considerably between the static and dynamic scenarios, and were confirmed experimentally in phantoms. This suggests that the Arrhenius model can be used to predict dynamic changes in optical and thermal fields. An increase in temperature rise due to a decrease in light penetration within the coagulated region during ILP of the liver was also demonstrated. The kinetics of ILP are complex and nonlinear due to coagulation, which changes the tissue properties during treatment. These complex effects can be adequately modelled using an Arrhenius damage formulation.

1. Introduction

The use of optical fibres for interstitial light delivery was demonstrated in the early 1980s as a viable means of heating and destroying deep-seated tumours (Bown 1983). Complete destruction of tumours can be achieved if the coagulated volumes conform to the tumour. One of the limitations of interstitial laser photocoagulation (ILP) is that the lesions are small, ranging from 1 to 3 cm in diameter per fibre. The size of the lesion can be increased by using higher laser powers (Prudhomme *et al* 1994). However, this causes the peak temperature to reach and exceed the point of vaporization, which leads to potentially detrimental and poorly understood effects such as bubble formation and carbonization (charring) of the tissue and fibre tip (Wyman *et al* 1992).

The issue of tissue carbonization is controversial. It occurs near the fibre tip, resulting in greatly increased local absorption of light. This causes the fibre tip to act like a point heat source. A point source has been shown to produce more predictable and slightly larger damage volumes (Harries *et al* 1994; Wyman *et al* 1992), although the remaining carbonized core may be biologically undesirable. Also, prior to carbonization, the tissue undergoes vaporization and bubble formation. The process may cause increased interstitial tissue pressure and the occurrence of gas embolii. There are thus some potential risks associated with the process of charring, with limited benefit. Therefore, it is desirable to maximize the size of coagulation without inducing charring. In a clinical setting, charring can be avoided by ensuring that the maximum temperature, which occurs at the fibre tip, does not exceed the vaporization temperature. The maximum temperature depends upon optical, thermal and blood flow properties of tissues, irradiation geometry and the laser power used. At present it is very difficult to predict the laser power requirements that are necessary to achieve a maximum damage volume while avoiding carbonization effects.

A number of studies have been aimed at modelling and understanding the thermal response of tissue during ILP (Welch and van Gemert 1995, Wyman and Whelan 1994, Welch 1984, McKenzie 1990). The conventional models consist of calculating the light distribution, the temperature rise and the extent of thermal damage. Each stage requires information from the previous stage and from experimental measurements (or theoretical calculations) of tissue properties. A simplified approach to this problem provides a linear set of solutions in fluence and temperature rise, assuming the tissue properties are constant, from which thermal damage can be calculated. Many ILP models have employed this linear solution (Beacco *et al* 1994, Rastegar *et al* 1992; Kim *et al* 1996, Anvari *et al* 1994).

In reality, however, the elevation of tissue temperature changes tissue properties, which affect the subsequent course of the ILP procedure. Thermal (Duck 1990, Welch and van Gemert 1995), optical (Duck 1990, Jacques *et al* 1991, Pickering 1992, Pickering *et al* 1994, Jaywant *et al* 1993) and blood perfusion (Mordon *et al* 1997, Fahim and el-Sabban 1995, Salcman *et al* 1989, Brown *et al* 1988, Reinhold and Endrich 1986) properties of tissue are altered when the tissue is heated. Currently, nonlinear models exist which account for changes in optical properties (Rastegar *et al* 1992), changes in blood perfusion (Sturesson and Andersson-Engels 1996, 1997) or a combination of both (Whelan and Wyman 1999, Roggan and Müller 1995, London *et al* 1995, Kim *et al* 1995, Jacques *et al* 1996, Glenn *et al* 1996, Beacco *et al* 1994). However, there has been little experimental evidence to demonstrate the accuracy of these models. This is partly due to the difficulty of reproducing dynamic processes under controlled experimental conditions.

Various methods have been used to model the change in optical properties during heating. One method assumes that tissue optical properties are replaced by coagulated properties once a certain critical temperature is reached (Whelan and Wyman 1999, Roggan and Müller 1994, Beacco *et al* 1994). This is based upon the heuristic assumption that photocoagulation occurs at a critical temperature (60 °C) (Whelan and Wyman 1999, Roggan and Müller 1994). The majority of methods, however, use the Arrhenius damage model to describe the heat-induced effects on changes in optical properties (Glenn *et al* 1996, Rastegar *et al* 1992, Kim *et al* 1996, Roggan and Müller 1994, Beacco *et al* 1994).

The purpose of this paper is to validate the use of nonlinear models to describe dynamic tissue changes based upon the Arrhenius damage model. Specifically, the effects of changes in optical properties are examined. Hence, the work presented attempts to elucidate the effects of changes in optical properties alone. Controlled experimental studies are then conducted in optical phantoms which have similar thermal properties to tissue, and the measurements in both static and dynamic phantom systems are compared with simulation results. Finally, the model is used to investigate its potential use in ILP treatment planning of the liver. Liver, like the dynamic albumen phantom, undergoes a visible whitening change in optical properties as it coagulates. However, liver also has the additional influence of blood perfusion. Since during ILP treatment planning one is also concerned with choosing an appropriate laser power to ensure temperatures below the vaporization threshold, the model was used to investigate theoretically the dynamics of lesion formation during liver ILP.

2. Materials and methods

2.1. Mathematical modelling

An optothermal model of ILP consists of calculations of the light distribution, the temperature rise and the extent of thermal damage. The following sections describe the manner in which each stage has been implemented in our formulation.

2.1.1. Light distribution in tissue. The light emitted from an interstitial fibre was modelled as an isotropically radiating point source situated at the origin of a spherical coordinate system. Photon propagation from the source was described using radiative transport theory (Star 1995, Duderstadt and Hamilton 1976). Exact analytical solutions to the radiative transport equation have been found for only a few special cases (Star 1995, Wyman and Whelan 1994, Patterson *et al* 1991). However, if scattering processes dominate absorption in the medium, an approximation to the radiative transport equation can be applied (Star 1995, Patterson *et al* 1991, Duderstadt and Hamilton 1976). This is known as the light diffusion approximation:

$$-D\nabla^2\phi(r) + \mu_a\phi(r) = s(r) \tag{1}$$

with

ϕ = light fluence rate (W cm^{-2})
D = diffusion coefficient (cm^{-1}) $= [3(\mu_s' + \mu_a)]^{-1}$
s = source term (W cm^{-3})

where μ_a is the absorption coefficient in tissue and $\mu_s' = \mu_s(1 - g)$ is the reduced scattering coefficient. g is the anisotropy factor which incorporates the effects of directionally dependent scattering (Wyman *et al* 1989). The solution to equation (1) for an isotropic point source emitting P_0 watts within an infinite *homogeneous* medium is expressed as (Duderstadt and Hamilton 1976):

$$\phi(r) = \frac{P_0\exp(-\mu_{\text{eff}}r)}{4\pi Dr}. \tag{2}$$

This diffuse fluence component is also referred to as the diffuse photon flux. The additional unscattered (or primary) photon flux falls off at a faster rate $(1/r^2)$ and its contribution to ϕ was found to be negligible for depths within tissue greater than approximately the width of the fibre (Roggan and Müller 1995). The absorbed power density, assuming non-radiative de-excitations only, is expressed as (Welch 1984):

$$P(r) = \mu_a\phi(r). \tag{3}$$

2.1.2. Calculation of temperature rise. The absorption of light in tissue causes a local elevation in temperature. Tissue heat transfer due to the deposited light is described by the bioheat transfer equation. The bioheat transfer equation was first introduced by Pennes (1948) to model heat transfer in perfused tissue such that

$$\rho c\frac{\partial T(r, t)}{\partial t} = \nabla \cdot [(k\nabla T(r, t))] + P(r, t) - w_b c_b[T(r, t) - T_{\text{art}}] \tag{4}$$

where

T = temperature (°C)
ρ = density of tissue (kg cm^{-3})
c = specific heat of tissue (J kg^{-1} °C^{-1})
k = thermal conductivity of tissue (W cm^{-1} °C^{-1})
r = radial distance (cm)
t = time (s)
T_{art} = temperature of arterial blood (°C)
P = deposited light power (W cm^{-3})
w_b = volumetric perfusion rate (kg s^{-1} cm^{-3})
c_b = specific heat of blood (J kg^{-1} °C^{-1})

On the right-hand side, the first term is the thermal conduction; the second term is the absorbed power density from the optical source (Wyman *et al* 1992); the last term describes the convective effects of blood flow represented as a heat sink proportional to tissue perfusion (Pennes 1948) excluding the effects of large blood vessels (Kolios *et al* 1999). Note that for a phantom with no perfusion, w_b would be set to 0.

The spatial domain was taken from the radius of the fibre edge, r_f, to a position, $r = 5$ cm, sufficiently far into the tissue where changes in temperature were negligible. Due to the spherical symmetry of the problem, temperature elevation (as well as light distribution) was solved in the radial direction only. The boundary condition imposed at the fibre edge ($r = r_f$) was

$$\left. \frac{\partial T}{\partial r} \right|_{r=r_f} = 0. \tag{5}$$

This is based upon the assumption that the thermal gradient was radially symmetric. The boundary condition imposed at the fibre edge itself assumes that the fibre tip acts as an insulative material and therefore there is no energy flow in the direction of the fibre tip. The second boundary condition assumes that there is no temperature rise at a distance r sufficiently deep in the tissue. This corresponds to a temperature gradient of 0 for large r, or mathematically:

$$\left. \frac{\partial T}{\partial r} \right|_{r=r_{\text{large}}} = 0. \tag{6}$$

2.1.3. Thermal damage calculation. The temperature rise can cause irreversible thermal damage. According to the Arrhenius formulation, the degree of tissue damage can be quantified by the damage index, Ω:

$$\Omega(r, \tau) = \ln \left(\frac{C(r, 0)}{C(r, \tau)} \right) = \int_0^\tau A \, e^{-E_a/RT(r,t)} \, dt \tag{7}$$

where

    $\Omega =$ damage index (dimensionless)
    $E_a =$ activation energy (J mol^{-1})
    $A =$ frequency factor (s^{-1})
    $R =$ universal gas constant (J mol^{-1} K^{-1})
    $\tau =$ total heating time (s).

The activation energy E_a and frequency factor A are derived from thermodynamic variables, such as heat of activation ΔH and Gibbs free energy ΔG which describe reaction kinetics (Johnson *et al* 1974). They can be related to the denaturation process of proteins and other cellular constituents. The equation above indicates that the damage index, Ω, is the logarithm of the ratio of the initial concentration of undamaged tissue to the concentration after damage accumulated for the time interval $t = 0$ to $t = \tau$. Therefore, $\Omega = 1$ corresponds to the reduction in concentration of native molecules to 37% for a unimolecular system. However, in terms of thermal damage for tissue, Ω is a function of the observer's definition of damage. For example, Henriques was the first to employ the Arrhenius integral to describe complete cellular necrosis of the basal epidermis layer due to thermal injury.

The values for the damage parameters E_a and A are derived from published experimental data which relate temperature to a thermally induced effect such as cell death. Borrelli *et al* (1990) produced survival curves for baby hamster kidney (BHK) cells exposed to temperatures in the range 43.5 °C to 57.0 °C using a colony formation assay and calculated the Arrhenius damage parameters for cell death ($E_a = 5.064 \times 10^5$ J mol^{-1}, $A = 2.984 \times 10^{80}$ (s^{-1})).

These values were used since they describe cell death close to the coagulative temperature range. Hence, these rate parameters, along with the Arrhenius integral equation (7), were used to calculate cell death damage due to a temperature rise $T(r, t)$, for ILP simulations of the liver. Similarly, equation (7) also was used to determine the depth, r_0, at which changes in optical properties occurred. The rate parameters, A and E_a, that described the whitening process of albumen during thermal denaturation were used in this case.

2.1.4. Nonlinear effects of dynamic optical properties. Coagulation causes a change in the optical properties of tissue which include changes in absorption and reduced scattering coefficients depending on the tissue type. During ILP, this change manifests itself visually as an inner sphere of coagulated tissue surrounded by native uncoagulated tissue (Tracz *et al* 1992). The approach used to model this phenomenon was to solve the light diffusion approximation analytically for a system consisting of two concentric spheres of different optical properties. The use of an analytical solution to solve a two-layer system in spherical coordinates requires few mathematical operations to calculate the spatial distribution of light fluence. Using this method, the inner 'layer' or sphere represents the tissue which has coagulated around the tip, with coagulated optical properties (μ_{a1}, μ'_{s1} for $r < r_0$), surrounded by a second shell of native tissue (μ_{a2}, μ'_{s2} for $r > r_0$). The radius of the second shell extends to infinity to model the case of an unbounded outer region of native tissue (see figure 1).
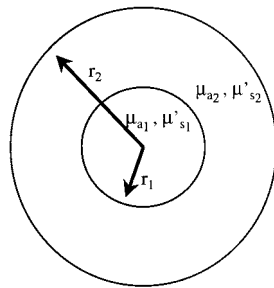

Figure 1. Schematic diagram of a two-layer case for solving the light diffusion approximation. Regions 1 and 2 represent the inner coagulated and outer native regions respectively. The boundary between the regions is r_0 which changes during the heating. The region r_2 extends to infinity, representing an unbounded region of native tissue.

This approach is less computationally intensive than the use of numerical methods which must discretize and solve the diffusion equation over the entire domain. Thus, this method was employed for ease of calculation and reduced computation time. There was qualitative agreement of this solution with an equivalent numerical solution performed by Whelan (1996). A general form of the analytical two-layer solution can be found in spherical coordinates (Star 1995) and in Cartesian coordinates (Vitkin *et al* 1995). The derivation of the specific form of the solution used in this paper is given in appendix A.

The solution of the two-layer case was calculated dynamically by continually recalculating the depth of coagulation from the Arrhenius damage integral (equation (7)) as heating progressed. The damage parameters were obtained from experimental values in the literature that measure the change of optical properties, μ_a and μ'_s, due to heat. The accumulated damage index close to the source is higher than that delivered deeper into tissue. Therefore, the coagulation front, r_0 was calculated according to the depth at which the damage index $\Omega(r, t)$ exceeds the mid-point between the native and coagulated states. That is, r_0 is the

location at which the concentration of native cells is such that

$$\Omega_{\text{opt}}(r_0, t) = \ln\left(\frac{1}{2}\right) \tag{8}$$

$$= \ln\frac{C(r_0, t)}{C(r_0, 0)} \tag{9}$$

where $C(r_0, 0)$ represents the initial concentration of native cells and $C(r_0, t)$ represents the concentration of native cells remaining at the boundary front, r_0. A ratio of these two values was chosen to be $\frac{1}{2}$ since the depth r_0 represents the midpoint boundary between the coagulated and native regions. Continued elevation of temperature with time causes the damage index to exceed the threshold at increasing depths of r_0. A new solution of the analytical two-layer model in spherical coordinates was generated with the advancement of the coagulation depth. This layer resulted in a time-varying absorbed light power density, $P(r, t)$. Changes in $P(r, t) = \mu_a \phi(r, t)$ affected future temperature calculations, $T(r, t + \Delta t)$, which in turn influenced $\Omega(r, t + \Delta t)$ and ultimately the next calculation of $\phi(r, t + \Delta t)$ and $P(r, t + \Delta t)$.

2.1.5. Numerical calculations using the finite difference method. The bioheat equation (4) was solved using the finite difference method (FDM). The FDM approximates differential equations by dividing the spatial and temporal domains into discretized points in space (nodes) and time (time steps). The continuous function derivatives of the bioheat equation are substituted with discrete finite differences. The central difference method was used, which was derived by the Taylor series expansion of derivatives, expressed as

$$T_i' = \frac{T_{i+1} - T_{i-1}}{2(\Delta r)} \tag{10}$$

$$T_i'' = \frac{T_{i+1} - 2T_i + T_{i-1}}{(\Delta r)^2}. \tag{11}$$

These equations are called the *central difference formulae*. Substitution of the central difference formulae into the bioheat equation in spherical coordinates for the independent variables, r and t gives:

$$\rho c \frac{T_{i,j+1} - T_{i,j-1}}{2(\Delta t)} = k\left(\frac{T_{i+1,j} - 2T_{i,j} + T_{i-1,j}}{(\Delta r)^2} + \frac{T_{i+1,j} - T_{i-1,j}}{r\Delta r}\right) + P_{i,j} - w_b c_b(T_{i,j} - T_{\text{art}}) \tag{12}$$

where i represents the spatial node index, j the time step index, Δr the node distance and Δt the difference between time steps. Thus, $T_{i,j}$ and $P_{i,j}$ are equivalent to the approximate value of temperature and deposited light power respectively at spatial position $i\Delta r$ and time step $j\Delta t$.

The explicit finite difference method was used to solve equation (12) (Croft and Lilley 1977). This method progresses forward in time calculating the next temperature value ($T_{i,j+1}$) using the temperatures at neighbouring nodes from the previous time step ($T_{i,j}$, $T_{i-1,j}$ and $T_{i+1,j}$). The process begins by assuming an initial condition of temperature $T_{i,0}$ for all values of i. The temperature profile for the first time step is then solved by rearranging (12) as follows:

$$T_{i,1} = T_{i+1,0}(F_0)\left(1 + \frac{\Delta r}{r}\right) + T_{i,0}\left(1 - 2F_0 - \frac{w_b c_b \Delta t}{\rho c}\right) \tag{13}$$

$$+ T_{i-1,0}(F_0)\left(1 - \frac{\Delta r}{r}\right) + \frac{\Delta t}{\rho c}(P_{i,0} + w_b c_b T_{\text{art}}) \tag{14}$$
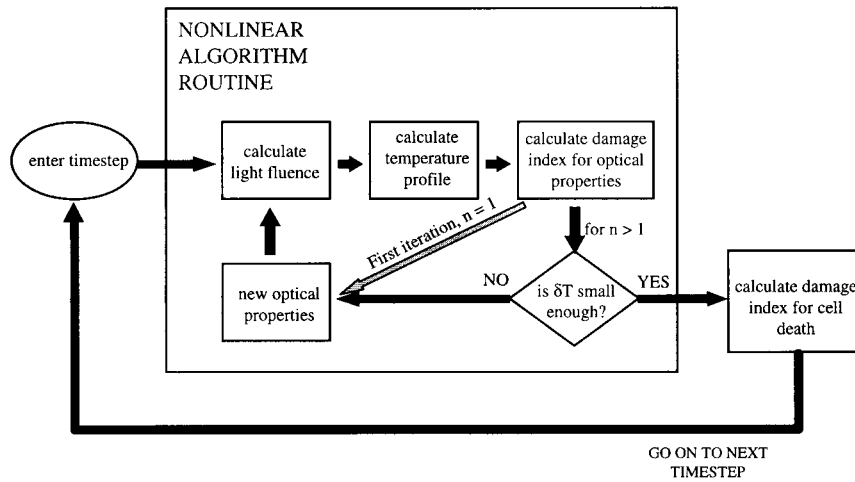
Figure 2. Flow chart of nonlinear algorithm that incorporates the effects of dynamic optical properties. *n* is the number of iterations performed per node and time step. The number of iterations was typically two to four.

where $F_0 = \frac{k}{\rho c}(\frac{\Delta t}{\Delta r^2})$ is called the *Fourier number*. The calculation is then repeated for all subsequent time steps. The final calculated values represent the *linear* solution of the bioheat equation.

2.1.6. Application of the finite difference method to nonlinear modelling. For the case of dynamic optical properties, the presence of a dynamic value of $P(r, t)$ which varies according to the extent of damage, required a modified finite difference approach to solve the *nonlinear* bioheat equation (Kim *et al* 1996). A flow chart of the steps is provided in figure 2 which is modified from Kim *et al* (1996). This approach first estimates the temperature by assuming initial (for the first time step) or previous (for all later time steps) values of the temperature-dependent properties (Patankar 1980). This initial temperature estimate was used to calculate the changes in the absorbed light pattern as described in section 2.1.4. The temperature was recalculated with the new conditions and compared with the first temperature estimate. If the difference between the two temperatures was within a tolerance of 0.1%, the updated temperature was stored and the program continued to the next time step. If the difference was larger, the second temperature was assumed to be the best estimate and another temperature comparison was made with the new values for the optical properties based upon the new best estimate in temperature. The pattern was repeated until the temperature comparison came within tolerance producing the temperature rise for that time step. Temperatures were calculated for all subsequent time steps in the same manner.

2.2. Numerical implementation and experimental validation

2.2.1. Model parameters. The theoretical model was used to predict temperature rise in optothermal phantoms consisting of albumen and polyacrylamide which were previously developed by Iizuka *et al* (1999). They include an albumen phantom with dynamic optical properties, a polyacrylamide phantom with static optical properties, with the equivalent values of μ_a and μ'_s of the albumen phantom in the native state and a polyacrylamide phantom with

Table 1. Biophysical properties of the albumen and polyacrylamide phantoms used in simulations. The thermal properties were based upon per cent water content according to approximations made by Spells (1960). The Arrhenius damage parameters were derived from the literature, based upon visual inspection (Pickering 1992). T_{crit} represents the critical temperature at which the damage index Ω is equal to unity after 10 min of heating. The optical properties ($\lambda = 805$ nm) of albumen of the native state were measured at room temperature and of the coagulated state after 45 min at 85 °C (Iizuka *et al* 1999).

Property	Albumen phantom	Reference	Polyacrylamide phantom
Water content W (% by mass)	86.8 ± 1	Iizuka *et al* (1999)	85.8 ± 1
Heat capacity c (J g^{-1} °C^{-1})	3.84 ± 0.02	Based upon W (Spells 1960)	3.82 ± 0.02
Conductivity k (W °C^{-1} cm^{-1})	$5.50 \pm 0.08 \times 10^{-3}$	Based upon W (Spells 1960)	$5.45 \pm 0.08 \times 10^{-3}$
Density ρ (g cm^{-3})	1.04 ± 0.01	Based upon W (Spells 1960)	1.04 ± 0.01
Activation energy E_a (J mol^{-1})	384 560	Pickering (1992)	n/a
Frequency factor A (s^{-1})	3.76×10^{57}	Pickering (1992)	n/a
Critical temperature T_{crit} (°C)	59.7	From E_a, A above	n/a
Native μ_a (cm^{-1})	0.50 ± 0.04	Iizuka *et al* (1999)	Same as albumen phantom
Coagulated μ_a (cm^{-1})	0.7 ± 0.1	Iizuka *et al* (1999)	Same as albumen phantom
Native μ_s' (cm^{-1})	2.67 ± 0.07	Iizuka *et al* (1999)	Same as albumen phantom
Coagulated μ_s' (cm^{-1})	13.1 ± 0.5	Iizuka *et al* (1999)	Same as albumen phantom
Native μ_{eff} (cm^{-1})	2.2 ± 0.2	Iizuka *et al* (1999)	Same as albumen phantom
Coagulated μ_{eff} (cm^{-1})	5.3 ± 0.6	Iizuka *et al* (1999)	Same as albumen phantom

equivalent static values of μ_a and μ_s' of the albumen phantom in the coagulated state. The albumen phantom consisted of chicken egg albumen, bacteriological agar and Naphthol Green dye. The polyacrylamide phantom, an optically transparent material in the near-infrared range, was combined with Intralipid-10% and Naphthol Green dye to achieve the equivalent scattering and absorptive properties of the albumen phantom for both the native and denatured states. The optical properties are listed in table 1 (Iizuka *et al* 1999). The thermal properties were estimated according to approximations based on the water content W by per cent mass (Spells 1960). The heat capacity c, thermal conductivity k, and density ρ of tissue can be approximated by:

$$c = 4.19(0.37 + 0.63W)(\text{J g}^{-1}\text{ K}^{-1}) \tag{15}$$

$$k = 4.19(0.133 + 1.36W) \times 10^{-3}(\text{W K}^{-1}\text{ cm}^{-1}) \tag{16}$$

$$\rho = 1.3 - 0.3W(\text{g cm}^{-3}). \tag{17}$$

Table 1 also includes the thermal properties of the albumen and polyacrylamide phantom based on their water content and equations (15) through (17). The thermal properties of water vary as a function of heating (Duck 1990). This variation was expected to affect the model predictions slightly. For example, there is 2.5% decrease in density and a 7.5% decrease in conductivity over a temperature range of 20 °C to 60 °C, while the heat capacity generally remains constant (Duck 1990). However, heat also dehydrates tissue, resulting in a drop in the percentage water content. Therefore, the temperature dependence of thermal properties of water is in the opposite direction to dehydration, as demonstrated by equations (15) to (17). Noting these compensating effects, error ranges based on the relative variation of properties and dehydration effects with temperature were heuristically chosen to be $\rho \pm 1\%$, $k \pm 1.5\%$ and $c \pm 0.5\%$.

The Arrhenius damage parameters of the coagulation process of albumen are also listed in table 1. Table 2 lists parameters for both the liver and phantom simulations. Note that the blood perfusion term w_b was set to 0 when solving the bioheat equation for the phantom experiments.

Table 2. Simulation parameters for the phantoms (polyacrylamide and albumen) and liver. The program continues to calculate thermal damage as the medium cools after the laser power has been shut off.

Physical parameter	Phantom	Liver
Fibre radius (μm)	750	200
Spatial domain (cm)	5	5
Time domain (min)	15	15
Node size dr (μm)	100	100
Timestep size dt (ms)	37	33
Cool down time (min)	5	5
Ambient temperature ($^\circ$C)	24	37
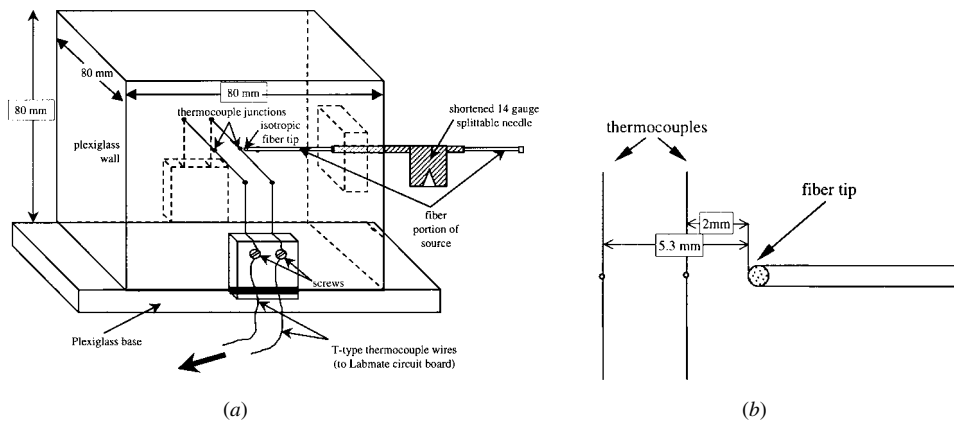
Figure 3. (*a*) Schematic diagram of apparatus used to measured the temperature rise within phantoms. (*b*) close-up of thermocouples and fibre tip.

2.2.2. Experimental set-up. The polyacrylamide and albumen phantoms were heated in a Plexiglass box with dimensions as shown in figure 3. A shortened 14-gauge needle was used to position the source fibre at the centre of the box face. With the box empty, a pair of type T thermocouples (IT-23, Physitemp, Clifton, NJ, USA), 3.3 mm apart and 0.076 mm in diameter, were pulled taut across the width of the box. The fibre tip was then positioned 2 mm from the first thermocouple. This was accomplished by placing the fibre in contact with the closest thermocouple and then retracting it by 2 mm with a micrometer translation stage. The box was filled with the phantom material (albumen, polyacrylamide with native optical properties or polyacrylamide with coagulated optical properties) and allowed to solidify, moulding to the source and the thermocouples (Iizuka *et al* 1999). Once cooled to room temperature, the phantom was heated at constant laser power using the Diomed-15 (Diomed Ltd, Cambridge, UK) laser at 805 nm for up to 20 min. The laser power setting could be adjusted in the range of 0.5 W to 15.0 W. However, due to a loss in power from coupling, the actual power deposited at the fibre tip was determined experimentally to be approximately 60% of the dial setting. Thermocouple readings were recorded every 2 s by a multifunction data acquisition system (Labmate Scienmetrics, Nepean, Ontario, Canada). The polyacrylamide phantom was cooled and re-heated at different laser powers. The albumen phantom exhibiting thermal denaturation was heated only once per phantom preparation.

Table 3. Biophysical properties used in the ILP simulation of the liver.

Property	Value	Reference
Heat capacity c (J g^{-1} $^{\circ}$C^{-1})	3.59	Duck (1990)
Conductivity k (W cm^{-1} $^{\circ}$C^{-1})	0.005 66	Duck (1990)
Density ρ (g cm^{-3})	1.05	Duck (1990)
Volumetric perfusion rate w_b (g s^{-1} cm^{-3})	0.0185[a]	
Heat capacity of blood c (J kg^{-1} $^{\circ}$C^{-1})	3.84[a]	
Temperature of blood T_{art} ($^{\circ}$C)	37	
Cell death E_a (J mol^{-1})	5.064×10^5	Borrelli *et al* (1990)
Cell death A (s^{-1})	2.984×10^{80}	Borrelli *et al* (1990)
Cell death T_{crit} ($^{\circ}$C)	44.7	Borrelli *et al* (1990)
Liver whitening E_a (J mol^{-1})	2.577×10^5	Jacques *et al* (1996)
Liver whitening A (s^{-1})	7.39×10^{37}	Jacques *et al* (1996)
Liver whitening T_{crit} ($^{\circ}$C)	58.2	Jacques *et al* (1996)
Native μ_a (cm^{-1})	0.30	Roggan *et al* (1995)
Coagulated μ_a (cm^{-1})	0.3	Roggan *et al* (1995)
Native μ_s' (cm^{-1})	10	Roggan *et al* (1995)
Coagulated μ_s' (cm^{-1})	31.8	Roggan *et al* (1995)
Native μ_{eff} (cm^{-1})	3.05	Roggan *et al* (1995)
Coagulated μ_{eff} (cm^{-1})	5.37	Roggan *et al* (1995)

[a] Perfusion value based upon: $\rho_b = 1.060$ g cm^{-3} (ICRP 1975) and a blood perfusion rate of 1100 ml min^{-1} kg^{-1} (Williams and Leggett 1989). The optical properties of liver pertain to a wavelength of 850 nm (Roggan *et al* 1995). T_{crit} is the critical temperature at which the damage index Ω is equal to unity after 10 min of heating.

2.3. Liver ILP simulation

The model was applied to a clinically relevant situation, laser thermal therapy of the liver. Currently ILP of the liver has been proposed for the palliative care of liver metastasis (Vogl *et al* 1997). Many patients who have metastatic spread to the liver have limited options for treatment. ILP provides a potential method of treating these tumours safely with minimal patient trauma. In order to deliver ILP effectively, simulations can be used to determine the most suitable pre-treatment parameters. There are numerous variables which can be altered such as laser power, heating time, fibre position and fibre tip design. The choice of such treatment parameters depends upon practical considerations as well as biophysical limitations such as avoiding high peak temperatures. For example, we chose a practical heating time of 15 min in our simulations of liver. Furthermore, carbonization of the fibre tip was avoided in the simulations by limiting the steady state temperature to be below vaporization by varying the laser power.

Simulations of ILP of the liver were conducted to determine if the effects of changes in optical properties seen with the albumen phantom would also be evident in tissue. However, liver simulations differed from those of the albumen phantom in that the liver simulations included the effects of blood perfusion where $w_b = $ constant. Thus, the Pennes bioheat formulation of equation (4) was applied for liver simulations, whereas only the basic heat transfer situation with $w_b = 0$ was used in the albumen simulations. Furthermore, the coagulation front of albumen represents the visible boundary between native and denatured egg white. In a clinical situation, however, cell death is a more relevant marker of tumour destruction. Therefore, the liver simulations examined the depth of cell damage as opposed to visible coagulative changes in optical properties as performed in the albumen phantom.

The thermal, optical and damage properties of liver were obtained from the literature and are listed in table 3. The other simulation parameters used in the model for liver are listed in table 2.

3. Results

3.1. Albumen and polyacrylamide phantoms

The model was tested with experimental measurements of temperature rise at distances of 2 mm and 5.3 mm from the fibre tip in albumen and polyacrylamide phantoms. The results of the nonlinear model with changing optical properties were confirmed in the albumen phantom, whereas the polyacrylamide phantom confirmed the linear model for static optical properties (native and denatured).

The temperature profiles measured at the 5.3 mm thermocouple in the static polyacrylamide phantoms are shown in figure 4, along with the simulation results. The error bars of the numerical predictions account for the error in the thermal properties (see section 2.2.1), the measured fibre coupling efficiency (± 0.04 watts, based upon a standard deviation of 30 repeated measurements of power at 1 W nominal setting) and the measured thermocouple positions ($r \pm 0.1$ mm). The temperature measurements in the polyacrylamide phantom mimicking the coagulated albumen were higher than in the polyacrylamide with native albumen, due to a difference in the light penetration. More light was absorbed close to the fibre for the coagulated phantom than the native phantom. The experimental results agreed well with predicted values for both the coagulated and native states at 5.3 mm and at 2 mm (results for the latter not shown).

Figure 5 shows the temperature rise measured in the albumen phantom at the two thermocouple locations. Numerical predictions are plotted for distances of 0 mm, 2 mm and 5.3 mm from the fibre edge. The most salient feature of the albumen phantom measurements was the increase in temperature at the 2 mm thermocouple which occurred at approximately 10 min. According to the numerical model, this increase corresponds to the onset of coagulation and was determined to occur at 9.75 min of heating. Another less pronounced temperature rise at the 5.3 mm thermocouple occurred approximately 1 min later. The delayed increase in temperature at the 5.3 mm position was a result of thermal conduction. The model accurately predicted the change in the rate of temperature rise at both thermocouple positions.

At around 14 min of heating the rate of temperature rise decreases slightly for the 2 mm thermocouple. This slight decrease deviated from our model predictions. This may be explained by the presence of high temperatures at the fibre edge as indicated by the top curve of figure 5. Vaporization of water begins at these high temperatures. This phase change may have caused additional changes in thermal and optical properties not accounted for in the model. For example, a change in thermal conductivity could result from dehydration of the phantom. The presence of bubbles due to vaporization may also increase the optical scattering coefficient and hence μ_{eff}. Consequently, the penetration depth would be reduced. This would cause an increase in temperature close to the tip, but at a distance of 2 mm this may appear as a drop in temperature due to the reduced penetration of light.

Figure 6 is a photograph of the final thermal lesion of the albumen phantom, cut at the $r = 0$ plane, showing a demarcation between coagulated and native albumen. However, a small transition region of approximately 2–3 mm was also observed. The location of the midpoint of the transition region is approximately 4 ± 1 mm from the fibre tip edge. This is within the range of the predicted value of 3.5 mm according to the Arrhenius integral at a depth when the concentration of the coagulated albumen is 50% ($\Omega = \ln(\frac{1}{2})$).
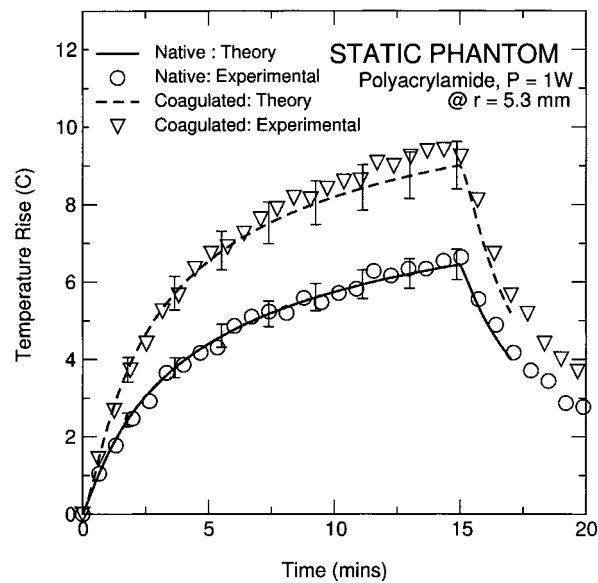
Figure 4. Temperature rise in polyacrylamide phantom with static optical properties. Thermocouple probe measurements at $r = 5.3$ mm with theoretical predictions for polyacrylamide phantom with the optical properties of native (lower curve) and coagulated (upper curve) albumen phantom. Error bars represent the error in numerical prediction based on uncertainty in thermal property value, fibre coupling efficiency and thermocouple positions.

Finally, figure 7 shows the temperature rise for the albumen phantom and for the polyacrylamide with the same optical properties of albumen in the native state. The power setting and heating time were chosen to ensure that no coagulation would occur in the albumen phantom. The temperature curves were very similar in shape and value for the two systems at both thermocouple positions. This suggests that the optical properties of the albumen phantom are well matched in the polyacrylamide material and that albumen, prior to the onset of coagulation, behaves in a linear fashion as seen with static optical properties.

3.2. ILP of the liver

Simulations were performed to compare the effects of dynamic optical properties with those of static optical properties during clinical ILP. In these simulations the laser power was adjusted such that the peak temperature at the fibre tip was just below the vaporization threshold (97 °C, or 60 °C above body temperature) at the end of the thermal therapy.

3.2.1. Temperature rise. Figure 8 shows the peak temperature rise at the location of the fibre edge, r_f. Coagulated tissue absorbs more light than native tissue resulting in a higher peak temperature close to the fibre tip due to the greater probability of absorption in the presence of increased scattering. Therefore less laser power (1.84 W) was required to heat coagulated tissue to the same peak temperature as native tissue (3.88 W). The dynamic case required lower power than constant native optical properties and a higher power than constant coagulated optical properties (2.11 W). This was expected since the dynamic model contains regions of coagulated and native tissue.
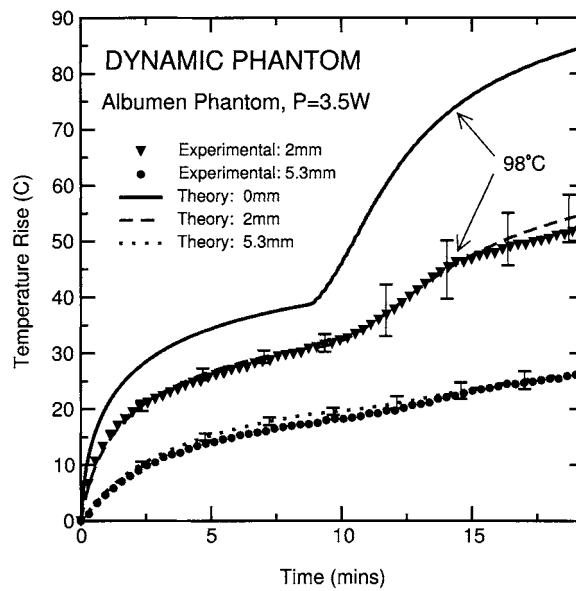
Figure 5. Temperature rise in albumen phantom with dynamic optical properties. Thermocouple probe measurements at $r = 2$ mm and $r = 5.3$ mm are compared with theoretical predictions at $r = 2$ mm, $r = 5.3$ mm and $r = r_f$ (fibre edge) for the albumen phantom after 19.5 min of heating. At $t \simeq 10$ min, there is a sharp increase in temperature at the 2 mm thermocouple due to the onset of coagulation. At $t \simeq 15$ min, the theoretical and experimental curves at $r = 2$ mm begin to exhibit a slight discrepancy; according to the model, the temperature at $r = 0$ mm reaches $\simeq 98\,°C$ at that time. Error bars represent error in numerical prediction based on uncertainty in thermal property value, fibre coupling efficiency and thermocouple positions.
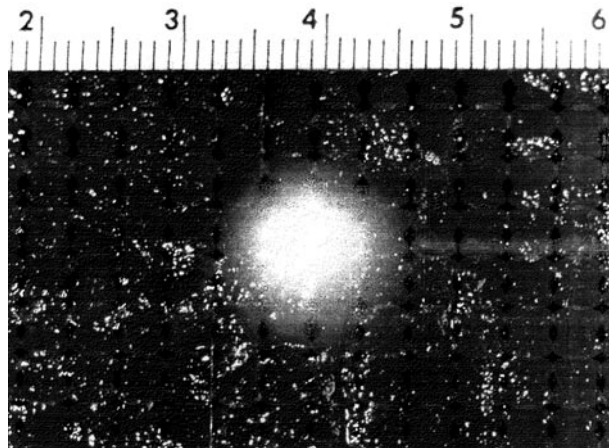

Figure 6. Photograph of thermal lesion formed in albumen phantom after 3.5 W at 19.5 min: top view.

For the static cases, the rate of temperature rise for the coagulated and native tissue did not differ greatly from the dynamic model, provided the laser power is scaled appropriately. Although the tissues were initially native in the dynamic model, the rate of temperature rise was slower than that of the native static case because of the lower laser power required (2.11 W
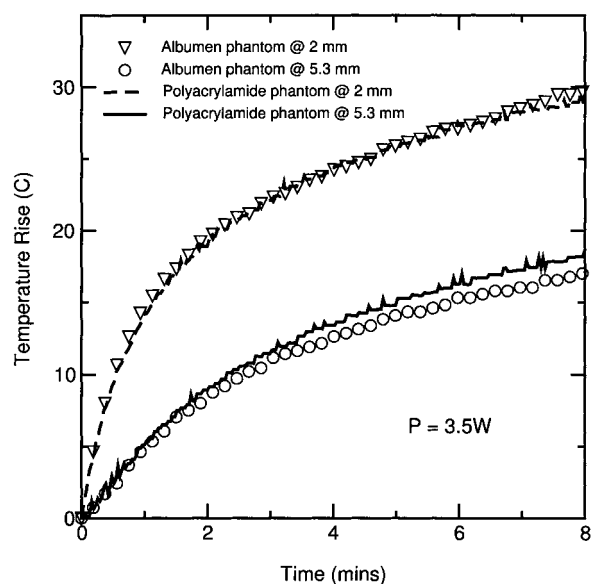
Figure 7. Thermocouple measurements at $r = 2$ mm and $r = 5.3$ mm for polyacrylamide (with native albumen properties) and albumen phantoms.
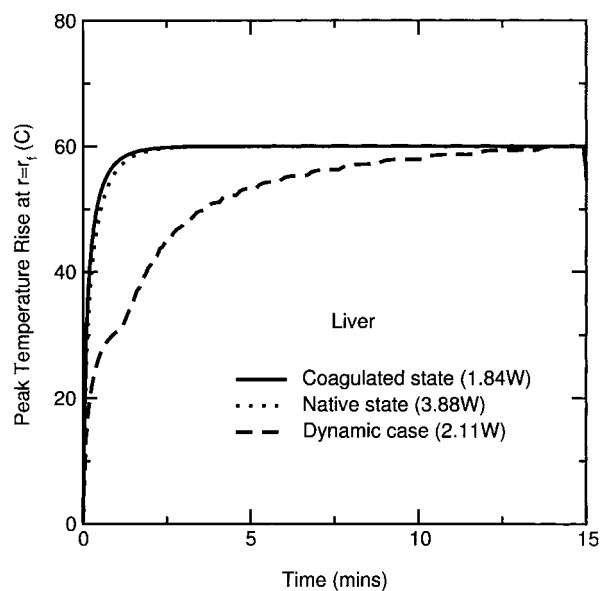

Figure 8. Simulation results for liver showing the effects of optical properties on temperature rise. The power is scaled such that the final temperature at the fibre edge (r_f) is just below vaporization (97 °C) after 15 min of heating. The native and coagulated cases with static optical properties yield the same peak temperature profile but require different laser powers. The dynamic case, however, exhibits a sudden change in temperature rise due to the onset of coagulation and requires a power level which is in between the static and dynamic values.

versus 3.88 W). The temperature rise decelerated and approached steady state. However, at approximately 1 min, the onset of coagulation caused a sudden increase in the rate of
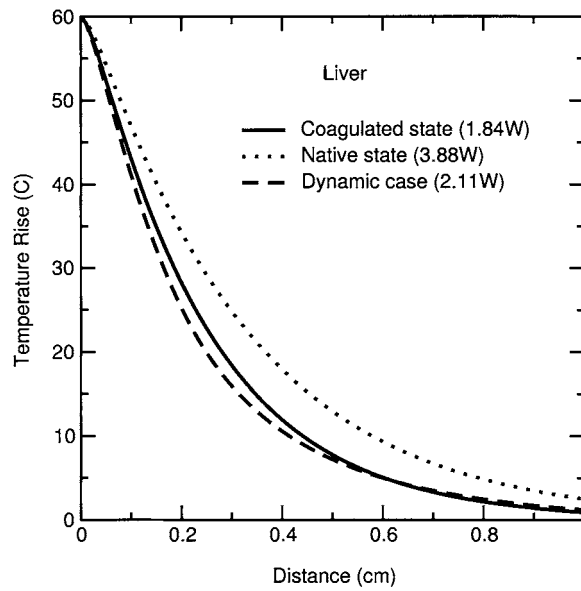
Figure 9. Temperature profiles from liver simulations. The power is scaled such that the final temperature at the fibre edge (r_f) is just below vaporization (97 °C) after 15 min of heating. The dynamic case has a similar temperature profile to the coagulated case. The temperature profile of the native case extends considerably deeper into tissue.
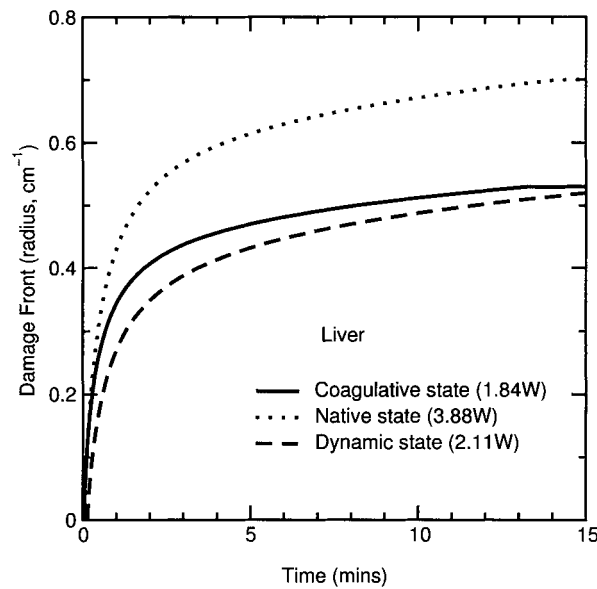

Figure 10. Damage front (radius) from liver simulations. The power is scaled such that the final temperature at the fibre edge (r_f) is just below vaporization (97 °C) after 15 min of heating. The damage front extends significantly deeper for the static native case. The coagulated and dynamic situations produce similar depths of damage.

temperature rise. The increase resulted from the rise in fluence close to the fibre tip due to the onset of coagulation. This effect was also observed experimentally in the albumen phantom

(see figure 5). The rate of temperature rise after coagulation in the dynamic case was slightly lower than that for the initial rate.

The spatial temperature profile at the end of the 15 min therapy is plotted in figure 9. The temperature elevation extended deeper into tissue for the native liver case than for the coagulated and the dynamic models. For the case of dynamic optical properties, the temperature gradient close to the fibre tip was larger than the static model cases. Further away from the tip ($\simeq 2$ mm), the temperature profile of the dynamic model was more gradual than the static cases.

3.2.2. Damage front. Figure 10 shows the effect of dynamic modelling on thermal damage leading to cell death where the Arrhenius damage index Ω is unity. The static model with native properties predicted the greatest depth of cell damage (7 mm). The static model with coagulated properties gave a lower prediction of 5.3 mm. The propagation of the damage front for the dynamic case started slightly later in time. Initially the rate of damage was slower than the static coagulated case. After the onset of coagulation, however, the rate increased until the final depth was virtually equal to that for static coagulated optical properties.

4. Discussion

Heating of biological media induces changes in optical properties which then influence light distribution within the media, in turn affecting the temperature rise. Thermal models of ILP have previously been developed which attempt to account for the effects of changes in optical properties (Whelan and Wyman 1999, Kim *et al* 1996, Rastegar *et al* 1992). Many investigators have assumed that these dynamic effects can be quantified using an Arrhenius damage model in which heat-induced changes in optical properties are related to the structural alterations due to the temperature rise (Kim *et al* 1996, Rastegar *et al* 1992). However, a direct comparison between the static and dynamic model assumptions based on the Arrhenius theory has not been well established experimentally. Therefore, it is important to test these assumptions which are the crucial mathematical link between the changes in light fluence, temperature rise and resultant damage.

We have developed a nonlinear model which incorporates the Arrhenius damage formulation to describe dynamic changes in tissue optical properties during heating. This was accomplished by using an analytical solution of the diffusion approximation. The analytical solution assumed that coagulated tissue can be represented as a system with two concentric layers where the inner sphere surrounding the fibre tip possesses coagulated optical properties and the outer region possesses native properties. The two-layer formulation yields a closed-form analytical optical solution that is readily programmable to define the spatial distribution of light fluence. This is less computationally intensive than using numerical methods which must discretize and solve the diffusion equation over the entire two-region domain. Therefore, the derived solution to the light diffusion approximation offers a fast and direct means of modelling light distribution in optothermal models.

A limitation of diffusion theory is that the accuracy close to the source and to tissue boundaries is questionable (Hielscher *et al* 1998, Roggan and Müller 1995). The accuracy improves deeper into tissue, away from the boundaries and the sources, due to the increased number of scattering events which engender the diffusion regime. This suggests that the peak temperature prediction at the fibre edge in our simulations may be inaccurate. However, Roggan and Müller (1995) demonstrated that diffusion theory agrees well with Monte Carlo predictions in tissue-like media for radial distances greater than the radius of the interstitial

applicator. Hence, the diffusion approximation can be used effectively to predict light fluence for practical distances away from the light source.

Validation of the model was performed by measuring the temperature rise and by visual inspection of the lesion in an albumen phantom with dynamic optical properties. Temperature measurements were obtained at distances of 2 and 5.3 mm away from the fibre tip using thin thermocouples. Positioning of the thermocouples was chosen to be as close to the fibre tip as possible where the features of coagulation could be observed while attempting to avoid excessive perturbation of the light field and self-heating of the thermocouples. Self-heating is caused by local absorption of the light by the thermocouple. We minimized this self-heating error by using small thermocouples (0.076 mm in diameter). In general, temperature measurements close to the fibre tip were sensitive to both self-heating as well as positional errors due to the presence of large thermal gradients (5–10 °C mm^{-1}) in this region. Nonetheless, the rapid elevation in temperature that was observed by the 2 mm thermocouple agreed well with theoretical predictions.

Recently there have been attempts to simulate dynamic changes in tissue properties during thermal therapy with lasers (Whelan and Wyman 1999, Kim *et al* 1996, Rastegar *et al* 1992). Many models address the issue by including multiple factors that affect lesion formation simultaneously. For example, they may include effects of both dynamic changes in blood perfusion and optical properties (Glenn *et al* 1996, Jacques *et al* 1996, Kim *et al* 1996, Roggan and Müller 1994, London *et al* 1995, Beacco *et al* 1994) which are difficult to verify experimentally, mostly as a result of the challenges of examining changes in blood perfusion during ILP. We have made a first step by examining the effects of dynamic changes in optical properties alone. Furthermore, we have simplified the problem by using an isotropic source and deriving an analytical solution within the framework of the well established theories of the light diffusion approximation. The experimental results in the albumen system agreed well with theory, which supports the use of the Arrhenius damage formulation to describe dynamic changes of tissue properties.

The model was used to simulate clinical ILP of the liver. Few studies analysed their results while limiting peak temperatures to avoid vaporization (Whelan *et al* 1995), a clinically relevant limitation. The dynamic model predicted a pronounced increase in temperature rise after the onset of coagulation, as confirmed in the albumen experiments. Rastegar *et al* (1992) have theoretically predicted a similar change in temperature rise for short irradiation times. However, this effect was not observed in several other laser irradiation studies which investigated the role of changing optical properties (Glenn *et al* 1996, Kim *et al* 1996, Beacco *et al* 1992, Roggan and Müller 1995). The reason for this may be due to the choice of fibre tip applicators, such as cylindrically diffusing tips, which differ from the isotropic source of our study (Glenn *et al* 1996, Kim *et al* 1996, Beacco *et al* 1992). The fluence rate profiles in liver for the dynamic case produced sharp temperature gradients within the coagulated regions close to the fibre tip. The gradient became less sharp in the native tissue regions deeper into tissue. The final damage volume was only slightly less than the model results calculated assuming constant coagulated optical properties. Therefore, the static system with coagulated optical properties may be proposed as a simplifying model for solving the more complex dynamic case. However, this may be inaccurate in terms of predicting temperature profiles *and* determining the necessary power levels.

It is important to include the dynamic effects of changing optical properties in optothermal models, for several reasons. First, the largest impact is on temperature predictions close to the fibre tip. Therefore dynamic models are essential to successfully ensure that vaporization at the fibre applicator has been avoided. Secondly, the significant change in temperature due to the onset of coagulation may provide additional information during the treatment. For

example, it may be used as a marker indicating the depth of the coagulation front or as a feedback parameter during the treatment. Finally, the nonlinear model improves the understanding of the significance of changing optical properties during thermal lesion formation. This information will be necessary when customizing treatments based on tissue type which have varying degrees of changes in μ_a and μ_s' due to heat, as would be the case in thermal therapy treatment planning or the on-line control of thermal therapy.

5. Conclusions

A nonlinear mathematical model was developed which uses the Arrhenius damage formulation to account for the effects of thermally induced changes in optical properties. Experimental validation was performed by measuring the temperature rise in albumen and polyacrylamide phantoms and comparing them with simulation results. The model agreed well with experimental measurements of temperature and damage in the albumen phantom, demonstrating that the Arrhenius formulation can be used in optothermal models to accurately predict the effects of changes in optical properties. The results indicate that changes in optical scattering coefficient cause an increase in the fluence gradients within the coagulated region of tissue surrounding the fibre tip. Thermal changes increase scattering, thus enhancing the probability of absorption in the coagulated regions close to the fibre, manifested as a notable increase in peak temperature rise at the onset of coagulation. The rapid elevation in temperature due to the dynamic changes in optical properties has the largest impact on peak temperature predictions close to the fibre tip. However, this temperature rise is also seen in deeper regions of tissue as a result of thermal conduction. This information may be important in order to avoid vaporization and charring. The final damage volume calculated for the dynamic optical properties was similar to predictions for static coagulated optical properties. However, the laser power requirements differ considerably for the dynamic and static scenarios.

Acknowledgments

Appendix. Two-layer solution to the diffusion approximation

The total light fluence in tissue can be described as the sum of the collimated and the diffuse photon contributions. The diffuse photon fluence rate is obtained by adding the particular, ϕ_p, and homogeneous, ϕ_h, solutions of the light diffusion approximation in the radial direction, r. Thus, the total fluence rate is

$$
\begin{aligned}
\phi_{\text{total}} &= \phi_{\text{diffuse}} + \phi_{\text{collimated}} \\
&= \phi_h + \phi_p + \phi_{\text{collimated}} \\
&= \phi_h + \phi_p + \frac{P_0}{4\pi r^2} \exp(-\mu_{\text{tr}}' r)
\end{aligned}
\tag{A.1}
$$

where P_0 is the total power of the source in watts and $\mu_{\text{tr}}' = \mu_s' + \mu_a$ is the transport attenuation coefficient. The collimated fluence, $\phi_{\text{collimated}}$, is due to the contribution of straight path photons

that have not been extinguished by encountering absorption or scattering events. For the diffuse contribution, the general format of the diffusion equation in spherical coordinates is:

$$-D\frac{\partial^2(r\phi(r))}{\partial r^2} + \mu_a r\phi(r) = \mu_s'\phi_0\frac{\exp(-\mu_{tr}'r)}{r} \tag{A.2}$$

where

$$\phi = \text{fluence rate(W cm}^{-2})$$
$$\phi_0 = \frac{P_0}{4\pi}, \text{ where } P_0 \text{ is the total laser power (W)}$$
$$\mu_a = \text{absorption coefficient (cm}^{-1})$$
$$\mu_s' = (1-g)\mu_s = \text{ reduced scattering coefficient (cm}^{-1})$$
$$\mu_{tr}' = \text{ transport attenuation coefficient (cm}^{-1})$$
$$= \mu_s' + \mu_a$$
$$D = \text{ diffusion coefficient (cm}^{-1})$$
$$= [3(\mu_s' + \mu_a)]^{-1}.$$

The source term on the right-hand side represents the distribution of the first-scattered photons from the light source (Vitkin *et al* 1995). The homogeneous solution is obtained when the right-hand side of equation (A.2) is set to zero. This gives:

$$\phi_h(r) = A\frac{\exp(-\mu_{eff}r)}{r} + B\frac{\exp(+\mu_{eff}r)}{r} \tag{A.3}$$

where $\mu_{eff} = \sqrt{\mu_a/D}$ is the effective attenuation coefficient and A and B are the unknown coefficients of the solution.

The particular solution using the Green's function method gives:

$$\phi_p(r) = \mu_s'\frac{\phi_0}{2\mu_{eff}r}[\exp(\mu_{eff}r)E_1(\alpha r) - \exp(-\mu_{eff}r)E_1(\beta r)] \tag{A.4}$$

where

$$E_1(x) = \int_x^\infty \frac{\exp(-t)}{t}\,dt$$

and

$$\alpha = \mu_{tr}' + \mu_{eff} \text{ and } \beta = \mu_t' - \mu_{eff}. \tag{A.5}$$

A retrospective analysis of the diffuse particular term of equation (A.4) was performed using numerical methods, which showed that its contribution was negligible compared with the homogeneous contributions for realistic values of μ_a and μ_s' (equation (A.3)). Therefore, it was ignored in the calculation of fluence for the two-layer solution. Subsequently, the diffuse fluence rate in the first medium (the coagulated layer closest to the source) and second medium (the native medium extending to $r = \infty$) can be expressed as:

$$\phi_{h_1} = A_1\frac{\exp(-\mu_{eff_1}r)}{r} + B_1\frac{\exp(\mu_{eff_1}r)}{r} \qquad r < r_0 \tag{A.6}$$

$$\phi_{h_2} = A_2\frac{\exp(-\mu_{eff_2}r)}{r} + B_2\frac{\exp(\mu_{eff_2}r)}{r} \qquad r > r_0. \tag{A.7}$$

$B_2 = 0$ since the fluence in medium 2 must approach zero as r approaches ∞. Therefore the unknowns are: A_1, B_1 and A_2. These unknowns can be solved by imposing appropriate boundary conditions.

The boundary conditions for the diffuse fluence rate are (I) continuous fluence rate and (II) continuous photon current at $r = r_0$. The final condition (III) assumes an overall energy balance. Mathematically, these conditions are represented as:

(I) $\phi_1(r_0) = \phi_2(r_0)$

(II) $\phi_1'(r_0) = (D_2/D_1)\phi_2'(r_0)$

(III) $P_{\text{total}} = P_1 + P_2 = P_0.$

Therefore, the boundary conditions become:

(I) $\phi_1(r_0) = \phi_2(r_0) \Rightarrow$

$$A_1 \frac{\exp(-\mu_{\text{eff}_1}r_0)}{r_0} + B_1 \frac{\exp(\mu_{\text{eff}_1}r_0)}{r_0} = A_2 \frac{\exp(-\mu_{\text{eff}_2}r_0)}{r_0}$$

(II) $\phi_1'(r_0) = (D_2/D_1) \cdot \phi_2'(r_0) \Rightarrow$

$$A_1 \exp(-\mu_{\text{eff}_1}r_0)\left(\frac{-\mu_{\text{eff}_1}}{r_0} - \frac{1}{r_0^2}\right) + B_1 \exp(\mu_{\text{eff}_1}r_0)\left(\frac{\mu_{\text{eff}_1}}{r_0} - \frac{1}{r_0^2}\right)$$
$$= \frac{D_2}{D_1} A_2 \exp(-\mu_{\text{eff}_2}r_0)\left(\frac{-\mu_{\text{eff}_2}}{r_0} - \frac{1}{r_0^2}\right).$$

The third equation is the total energy balance of both diffuse and collimated photons such that:

$$P_0 = \int_0^{r_0} \mu_{a_1}(\phi_{h_1} + \phi_{\text{collimated}_1})\, dV + \tag{A.8}$$

$$\int_{r_0}^{\infty} \mu_{a_2}(\phi_{h_2} + \phi_{\text{collimated}_2})\, dV \tag{A.9}$$

for $dV = 4\pi r^2\, dr$ and where

$$\phi_{\text{collimated}_1} = \phi_{0_1} \frac{\exp(\mu_{\text{tr}_1}'r)}{r^2} \qquad\qquad r < r_0 \tag{A.10}$$

$$\phi_{\text{collimated}_2} = \phi_{0_2} \frac{\exp(-\mu_{\text{tr}_2}'(r - r_0))}{r^2} \qquad r > r_0.$$

Note that in medium 2, $\phi_{\text{collimated}_2}$ has been attenuated by $\phi_{0_2} = \phi_{0_1}\exp(-\mu_{\text{tr}_1}'r_0)$ as it passes through medium 1. Substituting and rearranging the diffuse (equations (A.6) through (A.7)) and the collimated solutions (equations (A.10) into (A.9)) yields

$$\mu_{a_1} A_1 \int_0^{r_0} \exp(-\mu_{\text{eff}_1}r)r\, dr + \mu_{a_1} B_1 \int_0^{r_0} \exp(\mu_{\text{eff}_1}r)r\, dr + \mu_{a_2} A_2 \int_{r_0}^{\infty} \exp(-\mu_{\text{eff}_2}r)r\, dr$$
$$= \frac{P_0}{4\pi} - \mu_{a_1} \int_0^{r_0} \phi_{0_1} \exp(-\mu_{tr_1}'r)\, dr - \mu_{a_2} \int_{r_0}^{\infty} \phi_{0_2} \exp(r_0\mu_{\text{tr}_2}')\exp(-\mu_{\text{tr}_2}'r)\, dr. \tag{A.11}$$

Using the three boundary conditions (equations (I), (II) and (A.11)) yields a set of equations which can be solved with matrix operations:

$$\vec{Y} = \vec{F}\vec{X} \tag{A.12}$$

with

$$X = \begin{bmatrix} A_1 \\ B_1 \\ A_2 \end{bmatrix} \qquad \text{and} \qquad Y = \begin{bmatrix} 0 \\ 0 \\ \gamma(r) \end{bmatrix}$$

where $\gamma(r)$ is obtained from the right-hand side of (A.11) and is equal to:

$$\gamma(r) = \frac{P_0}{4\pi} + \frac{\mu_{a_1}\phi_{0_1}}{\mu_{tr_1}'}[\exp(-\mu_{\text{tr}_1}'r_0) - 1] - \frac{\mu_{a_2}\phi_{0_2}}{\mu_{\text{tr}_2}'}. \tag{A.13}$$

The matrix F is equal to:

$$\begin{bmatrix} \dfrac{\exp(-\mu_{\text{eff}_1}r_0)}{r_0} & \dfrac{\exp(\mu_{\text{eff}_1}r_0)}{r_0} \\[2mm] \exp(-\mu_{\text{eff}_1}r_0)\left(\dfrac{-\mu_{\text{eff}_1}}{r_0}-\dfrac{1}{r_0^2}\right) & \exp(\mu_{\text{eff}_1}r_0)\left(\dfrac{\mu_{\text{eff}_1}}{r_0}-\dfrac{1}{r_0^2}\right) \\[2mm] \mu_{a_1}\left[\dfrac{\exp(-\mu_{\text{eff}_1}r_0)}{-\mu_{\text{eff}_1}}\left(r_0-\dfrac{1}{-\mu_{\text{eff}_1}}\right)+\dfrac{1}{\mu_{\text{eff}_1}^2}\right] & \mu_{a_1}\left[\dfrac{\exp(\mu_{\text{eff}_1}r_0)}{\mu_{\text{eff}_1}}\left(r_0-\dfrac{1}{\mu_{\text{eff}_1}}\right)+\dfrac{1}{\mu_{\text{eff}_1}^2}\right] \end{bmatrix}$$

$$\begin{bmatrix} \dfrac{-\exp(-\mu_{\text{eff}_2}r_0)}{r_0} \\[2mm] \dfrac{D_2}{D_1}\exp(-\mu_{\text{eff}_2}r_0)\left(\dfrac{-\mu_{\text{eff}_2}}{r_0}-\dfrac{1}{r_0^2}\right) \\[2mm] \mu_{a_2}\left[\dfrac{\exp(-\mu_{\text{eff}_2}r_0)}{-\mu_{\text{eff}_2}}\left(\dfrac{1}{-\mu_{\text{eff}_2}}-r_0\right)\right] \end{bmatrix}.$$

The coefficients, A_1, B_1 and A_2 can then be obtained using ordinary matrix operations. The determined coefficients are then substituted back into the original equation for fluence (equations (A.6) through (A.7)) to give the net fluence, which comprises both collimated and diffuse contributions.

References

Anvari B, Rastegar S and Motamedi M 1994 Modeling of intraluminal heating of biological tissue: Implications for treatment of benign prostatic hyperplasia *IEEE Trans. Biomed. Eng.* **41** 854–63

Beacco C, Mordon S and Brunetaud J 1992 Development and experimental *in-vivo* evaluation of mathematical modeling of coagulation by laser *Proc. SPIE* **1646** 138–49

——1994 Development and experimental *in vivo* validation of mathematical modeling of laser coagulation *Lasers Surg. Med.* **14** 362–73

Borrelli M, Thompson L, Cain C and Dewey W 1990 Time–temperature analysis of cell killing of BHK cells heated at temperatures in the range of 43.5 °C to 57.0 °C *Int. J. Radiat. Oncol. Biol. Phys.* **19** 389–99

Bown S G 1983 Phototherapy of tumours *World J. Surg.* **7** 700–9

Brown S, Hunt J and Hill R 1988 A comparison of the rate of clearance of xenon and pertechnetate ion in murine tumors and normal leg muscles *Nucl. Med. Biol.* **15** 381–90

Croft D and Lilley D 1977 *Heat Transfer Calculations using Finite Difference Equations* 1st edn (Essex: Applied Science Publishers)

Duck F 1990 *Physical Properties of Tissue, Complete Reference Book* (London: Academic)

Duderstadt J and Hamilton L 1976 *Nuclear Reactor Analysis* (New York: Wiley)

Fahim M and el-Sabban F 1995 Hyperthermia induces ultrastructural changes in mouse plial microvessels *Anat. Rec.* **242** 77–82

Glenn T, Rastegar S and Jacques S 1996 Finite element analysis of temperature controlled coagulation in laser irradiated tissue *IEEE Trans. Biomed. Eng.* **43** 79–87

Harries S, Amin Z, Smith M, Lees W, Cooke J, Cook M, Schurr J, Kissin M and Bown S 1994 Interstitial laser photocoagulation as a treatment for breast cancer *Br. J. Surg.* **81** 1617–19

Hielscher A, Alcouffe E and Barbour R 1998 Comparison of finite-difference transport and diffusion calculations for photon migration in homogeneous and heterogeneous tissues *Phys. Med. Biol.* **43** 1285–302

ICRP 1975 Report of the task group on reference man *ICRP Publication* 23 (Oxford: International Commission on Radiological Protection)

Iizuka M, Sherar M and Vitkin I 1999 Optical phantom materials for near infrared laser photocoagulation studies *Lasers Surg. Med.* **25** 159–69

Jacques S, Newman C and He X Y 1991 Thermal coagulation of tissues: liver studies indicate a distribution of rate parameters, not a single rate parameter, describes the coagulation process *Advances in Biological Heat and Mass Transfer* (ASME) pp 71–3

Jacques S, Rastegar S, Thomsen S and Motamedi M 1996 The role of dynamic changes in blood perfusion and optical properties in laser coagulation of tissue *IEEE J. Sel. Top. Quantum Electron.* **2** 922–33

Jaywant S, Wilson B, Patterson M, Lilge L, Flotte T, Woolsey T and McCulloch C 1983 Temperature dependent changes in the optical absorption and scattering spectra of tissues: correlation with ultrastructure *Proc. SPIE* **1882** 218–28

Johnson F, Eyrina H and Stover B 1974 *The Theory of Rate Processes in Biology and Medicine* (New York: Wiley)

Kim B, Jacques S, Rastegar S, Thomsen S and Motamedi M 1995 The role of dynamic changes in blood perfusion and optical properties in thermal coagulation of the prostate *Proc. SPIE* **2391** 443–8

——1996 Nonlinear finite-element analysis of the role of dynamic changes in blood perfusion and optical properties in laser coagulation of tissue *IEEE J. Sel. Top. Quantum Electron.* **2** 922–33

Kolios M, Worthington A, Holdsworth D, Sherar M and Hunt J 1999 An investigation of the flow dependence of temperature gradients near large vessels during steady state and transient tissue heating *Phys. Med. Biol.* **44** 1479–97

London R, Glinsky M, Zimmerman G and Eder D 1995 Coupled light transport-heat diffusion model for laser dosimetry with dynamic optical properties *Proc. SPIE* **2391** 434–42

McKenzie A 1990 Physics of thermal processes in laser-tissue interaction *Phys. Med. Biol.* **35** 1175–209

Mordon S, Desmettre T, Devoiselle J and Soulie S 1997 Thermal damage assessment of blood vessels in a hamster skin flap model by fluorescence measurement of a liposome-dye system *Lasers Surg. Med.* **20** 131–41

Patankar S V 1980 *Numerical Heat Transfer and Fluid Flow* (Washington, DC: Hemisphere)

Patterson M, Wilson B and Wyman D 1991 The propagation of optical radiation in tissue I. Models of radiation transport and their application *Lasers Med. Sci.* **6** 155–68

Pennes H 1948 Analysis of tissue and arterial blood temperatures in the resting forearm *J. Appl. Phys.* **1** 93–122

Pickering J 1992 Optical property changes as a result of protein denature in albumen and yolk *J. Photochem. Photobiol. B: Biol.* **16** 101–11

Pickering J, Posthumus P and van Gemert J 1994 Continuous measurement of the heat-induced changes in the optical properties (at 1064 nm) of rat liver *Lasers Surg. Med.* **15** 200–5

Prudhomme M, Tang J, Rouy S, Delacretaz G, Salathe R and Godlewski G 1994 Diode laser and interstitial hyperthermia against ht29 colonic cancer. Effect of power settings on necrosis size *Proc. SPIE* **2327** 283–6

Rastegar S, Kim B and Jacques S 1992 Role of temperature dependence of optical properties in laser irradiation of biological tissue *Proc. SPIE* **1646** 228–31

Reinhold H and Endrich B 1986 Tumour microcirculation as a target for hyperthermia *Int. J. Hyperthermia* **2** 111–37

Roggan A, Dörschel K, Minet O, Wolff D and Müller G 1995 The optical properties of biological tissue in the near infrared wavelength range—review and measurements *Laser-Induced Interstitial Thermotherapy* 1st edn, ed G Müller and A Roggan (Bellingham, WA: SPIE Press) pp 10–44

Roggan A and Müller G 1994 2D computer simulations for real-time irradiation planning of laser-induced interstitial thermotherapy (LITT) *Proc. SPIE* **2327** 242–52

——1995 Dosimetry and computer based irradiation planning for laser-induced interstitial thermotherapy (LITT) *Laser-Induced Interstitial Thermotherapy* 1st edn, ed G Müller and A Roggan (Bellingham, WA: SPIE Press) pp 114–56

Salcman M, Moriyama E, Elsner H, Rossman H, Gettleman R, Neuberth G and Corradino G 1989 Cerebral blood flow and the thermal properties of the brain: a preliminary analysis *J. Neurosurg.* **70** 592–8

Spells K E 1960 The thermal conductivities of some biological fluids *Phys. Med. Biol.* **5** 1399–453

Star W 1995 Diffusion theory of light transport *Optical-Thermal Response of Laser Irradiated Tissue* ed A Welch and M van Gemert (New York: Plenum) pp 131–205

Sturesson C and Andersson-Engels S 1996 Theoretical analysis of transurethral laser-induced thermo-therapy for treatment of benign prostatic hyperplasia. Evaluation of a water-cooled applicator *Phys. Med. Biol.* **41** 445–63

——1997 Tissue temperature control using a water-cooled applicator: implications for transurethral laser-induced thermotherapy of benign prostatic hyperplasia *Med. Phys.* **24** 461–70

Tracz R, Wyman D, Little P, Towner R, Stewart W, Schatz S, Pennock P and Wilson B 1992 Magnetic resonance imaging of interstitial laser photocoagulation in brain *Lasers Surg. Med.* **12** 165–73

Vitkin I, Wilson B and Anderson R 1995 Analysis of layered scattering materials by pulsed photothermal radiometry: application to photon propagation in tissue *Appl. Opt.* **34** 2973–82

Vogl T, Mack M, Straub R, Roggan A and Felix R 1997 Magnetic resonance imaging–guided abdominal interventional radiology: laser-induced thermotherapy of liver metastases *Endoscopy* **29** 577–83

Welch A 1984 The thermal response of laser irradiated tissue *IEEE J. Quantum Electron.* **20** 1471–81

Welch A and van Gemert M (ed) 1995 *Optical-thermal Response of Laser-irradiated Tissue* (New York: Plenum)

Whelan W 1996 Dynamic modeling of ILP in soft tissues *PhD Thesis* McMaster University, Hamilton, Ontario, Canada

Whelan W and Wyman D 1999 Modeling of interstitial laser photocoagulation: implications for lesion formation for liver *in vivo Lasers. Surg. Med.* **24** 202–8

Whelan W, Wyman D and Wilson B 1995 Investigations of large vessel cooling during interstitial laser heating *Med. Phys.* **22** 105–15

Williams L and Leggett R 1989 Reference values for resting blood flow to organs of man *Clin. Phys. Physiol. Meas.* **10** 187–217

Wyman D, Patterson M and Wilson B 1989 Similarity relations for the interaction parameters in radiation transport and their applications *Appl. Opt.* **28** 5243–9

Wyman D and Whelan W 1994 Basic optothermal diffusion theory for interstitial laser photocoagulation *Med. Phys.* **21** 1651–6

Wyman D, Whelan W and Wilson B 1992 Interstitial laser photocoagulation: Nd:YAG 1064 nm optical fibre source compared to point heat source *Lasers Surg. Med.* **12** 659–64